HHS Public Access

Author manuscript

Phys Med Biol. Author manuscript; available in PMC 2017 August 07.

Published in final edited form as:

Phys Med Biol. 2016 August 7; 61(15): 5639–5661. doi:10.1088/0031-9155/61/15/5639.

Respiratory motion correction in 4D-PET by simultaneous motion estimation and image reconstruction (SMEIR)

Faraz Kalantari[1], **Tianfang Li**[2], **Mingwu Jin**[3], and **Jing Wang**[1]

[1]Department of Radiation Oncology, UT Southwestern Medical Center, Dallas, Texas

[2]Department of Radiation Oncology, University of Pittsburgh Cancer Institute, Pittsburgh, Pennsylvania 15232

[3]Department of Physics, University of Texas at Arlington, Arlington, TX 76019, USA

Abstract

In conventional 4D positron emission tomography (4D-PET), images from different frames are reconstructed individually and aligned by registration methods. Two issues that arise with this approach are as follows: 1) the reconstruction algorithms do not make full use of projection statistics; and 2) the registration between noisy images can result in poor alignment. In this study, we investigated the use of simultaneous motion estimation and image reconstruction (SMEIR) methods for motion estimation/correction in 4D-PET. A modified ordered-subset expectation maximization algorithm coupled with total variation minimization (OSEM-TV) was used to obtain a primary motion-compensated PET (pmc-PET) from all projection data, using Demons derived deformation vector fields (DVFs) as initial motion vectors. A motion model update was performed to obtain an optimal set of DVFs in the pmc-PET and other phases, by matching the forward projection of the deformed pmc-PET with measured projections from other phases. The OSEM-TV image reconstruction was repeated using updated DVFs, and new DVFs were estimated based on updated images. A 4D-XCAT phantom with typical FDG biodistribution was generated to evaluate the performance of the SMEIR algorithm in lung and liver tumors with different contrasts and different diameters (10 to 40 mm). The image quality of the 4D-PET was greatly improved by the SMEIR algorithm. When all projections were used to reconstruct 3D-PET without motion compensation, motion blurring artifacts were present, leading up to 150% tumor size overestimation and significant quantitative errors, including 50% underestimation of tumor contrast and 59% underestimation of tumor uptake. Errors were reduced to less than 10% in most images by using the SMEIR algorithm, showing its potential in motion estimation/correction in 4D-PET.

1. INTRODUCTION

Positron emission tomography (PET) with fluoro-2-deoxy-D-glucose (FDG) has been used increasingly over the last two decades for the diagnostic evaluation and detection of metabolic and functional abnormalities of early-stage cancer (Gambhir *et al.*, 2001). In general, PET has higher sensitivity than computed tomography (CT) for the detection and staging of cancer (Toloza *et al.*, 2003; Chua *et al.*, 2007). Moreover, the incorporation of PET data into treatment planning improves lung tumor delineation by including positive

lymph nodes. Thus, PET data reduces the likelihood of geographic misses and improves the chance of achieving local control (Erdi *et al.*, 2002; Mah *et al.*, 2002).

Respiratory motion in the upper abdomen and chest areas during PET imaging leads to organ displacement (primarily lung and liver) and a reduction in quantitative and qualitative image accuracy, affecting subsequent diagnosis and treatment (Callahan *et al.*, 2014). The spatial resolution of current PET scanners is approximately equal to 3–5 mm full width half-maximum (FWHM). In contrast, the diaphragm typically moves about 15–20 mm due to respiration (Schwarz and Leach, 2000). In a clinical trial conducted on twenty patients, the motion of tumors in the lower lobes of the lung were found to be 12 ± 2 mm in the cranial-caudal direction (Seppenwoolde *et al.*, 2002), substantially reducing effective spatial resolution. Additionally, benefits gained by increasing the scanner resolution are known to be small unless motion correction is applied (Polycarpou *et al.*, 2014).

Respiration causes lesion smearing, image blurring and quality degradation, affecting the quantification of FDG uptake, target-to-background contrast, and the ability to define correct lesion size. Degrading effects of respiratory motion on lung and liver PET images have been widely examined. Erdi et al. showed that lung motion during PET acquisition may lead to incorrect tumor staging (Erdi *et al.*, 2004). The same group reported variation in tumor uptake during different respiratory phases due to the misregistration of PET and CT, and inaccurate attenuation correction in certain phases (Erdi *et al.*, 2004). Simulation studies have showed that respiratory motion-induced errors in tumor quantification and delineation highly depend on motion amplitude, tumor location, background activity and tumor size, with a 129% overestimation of volume for small liver tumors (Geramifar *et al.*, 2013; Park *et al.*, 2008). Severe artifacts have been reported for lesions near the lung base, where motion is more pronounced due to breathing (Cohade *et al.*, 2003; Geramifar *et al.*, 2013; Osman *et al.*, 2003; Park *et al.*, 2008).

Early attempts to compensate for respiratory motion in lung PET imaging focused on the external monitoring of patient breathing using external markers and video cameras (Erdi *et al.*, 2004; Nehmeh *et al.*, 2002) or external radioactive sources attached to the abdomen (Nehmeh *et al.*, 2003). In this method, only data within a specific breathing phase are reconstructed, excluding all other information, constituting a “selection of frames” rather than true motion correction (Nehmeh *et al.*, 2002; Nehmeh *et al.*, 2003). Gated-PET imaging has been suggested as a potential solution to compensate for respiratory motion effects. In the proposed method, the acquisition time is split into several intervals referred to as gates. In conventional 4D-PET methods, data from each individual gate is reconstructed to achieve motion-freeze images in different respiratory phases (Erdi *et al.*, 2004). However, every frame only contains a portion of all acquired data resulting in noisy reconstructed images. Post reconstruction registration (PRR) methods are alternatives that increase signal-to-noise ratio by using non-rigid registration approaches to align individual frames and calculate the average image to achieve motion compensated images (Dawood *et al.*, 2006; Dawood *et al.*, 2008). A higher number of gates results in improved motion freeze; however, a smaller portion of coincidence data in each gate leads to highly noisy frames, resulting in poor image quality for each reconstructed frame. Low quality images can cause inaccurate motion

estimates and alignment errors. For accurate image registration, this motion-correction technique requires a good contrast to noise for each gated image.

When motion vectors are available, superior correction methods will incorporate motion information within the reconstruction algorithms. This approach is broadly referred to as 4D reconstruction (Rahmim *et al.*, 2013). Motion vectors can be estimated from high quality 4D-CT images (Lamare *et al.*, 2007b; Li *et al.*, 2006; Qiao *et al.*, 2006). However, the use of 4D CT increases the dose that cannot be easily justified for all patient acquisitions (Matsuzaki *et al.*, 2013). In addition, differences between the corresponding gated frames in 4D PET and 4D CT have also been reported while using multimodality imaging devices, resulting in errors associated with the derivation of motion vectors from 4D CT frames for motion correction in PET (Goerres *et al.*, 2003; Lamare *et al.*, 2007a). The recent advent of PET/MR scanners allows dynamic MR imaging with higher contrast than 4D-CT for motion estimation (Manber *et al.*, 2015; Fayad *et al.*, 2015). In this approach, motion fields are estimated from concurrently acquired tagged MR images, using nonrigid image registration methods, and are incorporated into a PET list-mode reconstruction algorithm (Chun *et al.*, 2012). The described methods use all available projection data to reconstruct each individual frame (Guerin *et al.*, 2011). The main drawback is the need for complementary images from other modalities to estimate the motion model, while less attention is paid to motion estimation from raw PET data. Moreover, 4D PET-MR imaging requires integrated PET-MR scanners, complex pulse sequences and retrospective gating methods (Grimm *et al.*, 2015; Cai *et al.*, 2011).

More sophisticated motion compensation methods jointly estimate image and motion by including them in a cost function (Blume *et al.*, 2012; Jacobson and Fessler, 2003; Wang and Qi, 2015). They typically consider a motion-aware acquisition model that relates the projection data at different time frames to a single motion-free image. By optimizing this objective function, image and motion can be jointly estimated to fit into this model in the best possible way. In these methods, regularization is necessary for both image and motion.

We recently introduced a new technique for simultaneous motion estimation and image reconstruction (SMEIR) in 4D-cone beam CT (4D-CBCT) imaging (Dang *et al.*, 2015; Wang and Gu, 2013b). In this study, we investigated the use of the SMEIR method to estimate and correct motion in 4D-PET. The proposed algorithm estimates motion vectors in an iterative process by only using 4D-PET projection data. To estimate deformation vectors, the reference phase image is warped so that its projections fit those of other phases. By using the estimated deformation fields, a motion compensated 4D-PET image is reconstructed. This updated image is used as a reference image for next iteration of motion estimation.

2. METHODS

2-1. Generating 4D PET projections

A fast ray tracing algorithm was used to generate 3D-PET projections for a digital phantom by calculating the activity ray sum between different pairs of PET detectors (Han *et al.*, 1999; Siddon, 1985). The dimensions and geometry of the PET simulator were based on a real PET scanner composed of 52 rings with 624 4×4 millimeter detectors per ring. 3D-PET

projections of a time-varying digital phantom were considered as 4D-PET projections. Poisson noise was included to simulate noisy projections. Two different noise levels were studied in this work representing high and low count images. For low count projections, we assumed 20 million registered lines of responses (LORs) in each time frame, resulting in a total of 160 million registered events. This is a typical 5-minute data set for 3D-PET imaging of the chest region using FDG. For high count projections, however, we assumed 160 million registered event in each time frame. The reason for the use of high count imaging was to investigate the performance of PRR methods in low noise conditions compared with our SMEIR method.

2-2. Motion modeling in projections

The goal of our study was to identify a matrix equation that could relate all projection data to a reference image. We assumed $\boldsymbol{y^t}$ as the vector of the measured 4D-PET projections and $\boldsymbol{\lambda^t}$ as the vector of unknown activity voxel values in the object at phase t. Ignoring quantum noise, $\boldsymbol{\lambda^t}$ and $\bar{\boldsymbol{y}}^{\boldsymbol{t}}$ are related as follows:

$$\bar{\boldsymbol{y}}^{\boldsymbol{t}} = A\boldsymbol{\lambda^t} \quad (1)$$

where matrix A represents the forward projection matrix. The element a_{ij} of matrix A represents the probability to detect a photon emitted from the jth voxel to the ith detector pair. In our analytical projector, a_{ij} is the intersection length of projection ray i with voxel j and was calculated by the fast ray-tracing technique (Han *et al.*, 1999; Siddon, 1985).

We assume that any change in the object is purely caused by voxel displacement and not by activity redistribution over time. When a motion model is available to describe the motion between different phases, the object at any time frame is simply a warped version of the initial object and can be calculated as:

$$\boldsymbol{\lambda^t} = \boldsymbol{W}_{0\to t}\boldsymbol{\lambda^0} \quad (2)$$

where $\boldsymbol{W}_{0\to t}$ represents the warping operation to transform 4D-PET from phase 0 to phase t with $t \in [0,\ T-1]$ and T is the total number of phases. Conversely, $\boldsymbol{\lambda^0} = \boldsymbol{W}_{t\to 0}\boldsymbol{\lambda^t}$ transforms the phase t image to phase 0. Thus, mean projection values from any other phase $\bar{\boldsymbol{y}}^{\boldsymbol{t}}$ can be related to the 4D-PET at phase 0 by:

$$\bar{\boldsymbol{y}}^{\boldsymbol{t}} = \boldsymbol{A}\boldsymbol{W}_{0\to t}\boldsymbol{\lambda^0} \quad (3)$$

If $\boldsymbol{y}^* = (\boldsymbol{y^0}, \ldots, \boldsymbol{y^{T-1}})$ denotes the measured projections from all phases and $\boldsymbol{A}^* = (\boldsymbol{A}\boldsymbol{W}_{0\to 0}, \ldots, \boldsymbol{A}\boldsymbol{W}_{0\to T-1})$ presents the 4D projection matrix, Eq. (3) can also be expressed as:

$$\bar{y}^{*} = A^{*}\boldsymbol{\lambda}^{\mathbf{0}} \quad (4)$$

Thus, the projection from all phases can be used to reconstruct 4D-PET at reference phase 0. In this study, we refer to it as primary motion compensated PET (pmc-PET). With pmc-PET, all other phases of 4D-PET can be obtained according to Eq. (2).

2-3. pmc-PET image reconstruction

The number of measured counts in projections, **y**, is Poisson distributed. One widely used approach to solve equation 4 for PET image reconstruction is the maximum likelihood expectation maximization (MLEM) (Lange and Carson, 1984; Shepp and Vardi, 1982) or its faster version, the ordered subsets expectation maximization (OSEM) (Hudson and Larkin, 1994). These algorithms maximize the likelihood function and reconstruct image $\boldsymbol{\lambda}^{\mathbf{0}}$, which has the highest possibility to yield **y** (Bruyant, 2002; Lange and Carson, 1984). For the Poisson distribution, maximizing the log-likelihood is a standard method that results in the MLEM algorithm. By considering the deformation in the log-likelihood, the reconstruction seeks image $\boldsymbol{\lambda}^{\mathbf{0}}$ that maximizes the following objective function:

$$LL\left(\boldsymbol{\lambda}^{\mathbf{0}}\right) = \sum_{t} \boldsymbol{y}^{t} ln\left(\bar{\boldsymbol{y}}^{t}\right) - \bar{\boldsymbol{y}}^{t} = \sum_{t} \boldsymbol{y}^{t}\left(ln\left(\boldsymbol{A}\boldsymbol{W}_{0\to t}\boldsymbol{\lambda}^{\mathbf{0}}\right) - \boldsymbol{A}\boldsymbol{W}_{0\to t}\boldsymbol{\lambda}^{\mathbf{0}}\right) \quad (5)$$

By analogy to the standard MLEM algorithm, we employed a hybrid motion-incorporated algorithm for motion compensation in which voxel values were updated by the following relation (Li *et al.*, 2006; Qiao *et al.*, 2006; Rahmim *et al.*, 2010):

$$\boldsymbol{\lambda}^{0,(n+1)} = \boldsymbol{\lambda}^{0,(n)} \frac{1}{\Sigma_t \boldsymbol{W}_{0\to t}^{\mathrm{T}} \boldsymbol{A}^{\mathrm{T}} \mathbf{1}} \sum_{t} \boldsymbol{W}_{0\to t}^{\mathrm{T}} \boldsymbol{A}^{\mathrm{T}} \frac{\boldsymbol{y}^{t}}{\boldsymbol{A}\boldsymbol{W}_{0\to t}\boldsymbol{\lambda}^{0,(n)}} \quad (6)$$

In the above equation, n is the iteration number, **1** is a column vector with all elements equal to 1, $\boldsymbol{A}$ and $\boldsymbol{A}^{\mathrm{T}}$ represent the system matrix for forward and backprojection. $\boldsymbol{W}_{0\to t}$ and $\boldsymbol{W}_{0\to t}^{\mathrm{T}}$ are deformation matrix and its transpose respectively. In this equation, $\boldsymbol{y}^{t}$ is the projection data vector from any phase $t \in [1, T]$. Therefore, phase 0 image $\boldsymbol{\lambda}^{0}$ can be reconstructed using all projection data, assuming that the deformation vector fields (DVFs) between all phases and phase 0 are known. Although deformation has been shown in a matrix form for the ease of expression, in practice a warping function was used to deform the image from phase 0 to t using DVFs. The same warping function with inverse DVFs, that deforms the error matrix from phase t to 0, was used as a practical approximation of $\boldsymbol{W}_{0\to t}^{\mathrm{T}}$. Applying inverse operator instead of transpose of the deformation matrix for non-rigid transformation has been justified as an acceptable approximation for 4D-PET reconstruction (Li *et al.*, 2006). The second term in Eq. (6) defines the inverse deformation process that deforms the error determined by the projections at phase t to update the 4D-PET at phase 0. Since both forward and backward deformations are involved in updating $\boldsymbol{\lambda}^{\mathbf{0}}$ in equation (6), inverse

consistent deformation vector fields are required (Wang and Gu, 2013b). All images belonging to other phases can be easily determined by shifting the phase-0 image by equation 2 that describes the forward deformation process, transforming the phase 0 reconstructed image to phase *t*. Considering each phase projection as a subset increases the number of subsets by phase number factor. A higher number of subsets can speed up the convergence rate.

A motion model is required to begin the reconstruction. To find a reasonable motion model, all eight phases were reconstructed individually. In addition, the inverse consistent Demons deformable registration between phase 0 and all other phases was applied to obtain initial DVFs (Gu *et al.*, 2010; Thirion, 1998). A free software for non-rigid image registration with the Demons algorithm was used to obtain the initial forward and inverse DVFs (Kroon, 2008). Default software parameters were used for all the studies in this paper, including high and low count images and the physical phantom study. In brief, the limited memory Broyden–Fletcher–Goldfarb–Shanno (LBFGS) optimization method with a normal line search was used. Termination tolerance on the DVFs and the energy function value were both 10^{-6}. The maximum number of iterations allowed was 400, and the maximum number of function evaluations allowed was 100 times the amount of the unknowns. The initial DVFs were estimated based on individual noisy reconstructed frames and were not sufficiently accurate. Using Demons DVFs, a primary motion compensated PET (pmc-PET) for phase 0 was reconstructed from equation (5). Consequently, all other phases were calculated from equation (6). While the selection of the initial DVFs is arbitrary and can even be an array of zeros, choosing more realistic DVFs can speed up the convergence rate. In section 2–4 we discuss how the DVFs are updated during motion estimation. To suppress the noise, the total variation (TV) of reconstructed pmc-PET was minimized by the standard steepest descent method after every sub-iteration during OSEM reconstruction.

2-4. Motion estimation

The SMEIR algorithm can estimate and update motion vectors by matching updated image projections to those of other phases. In other words, it minimizes the cost functions f_1 and f_2 to find DVFs as follows:

$$\begin{aligned} f_1\left(\boldsymbol{v}^{\mathbf{0}\to t}\right) &= \left\| \boldsymbol{y}^{t} - \boldsymbol{A}\boldsymbol{\lambda}^{\mathbf{0}}\left(\boldsymbol{x}+\boldsymbol{v}^{\mathbf{0}\to t}\right)\right\|_{l2}^{2} + \beta\varphi\left(\boldsymbol{v}^{\mathbf{0}\to t}\right) \\ f_2\left(\boldsymbol{v}^{t\to \mathbf{0}}\right) &= \left\| \boldsymbol{y}^{\mathbf{0}} - \boldsymbol{A}\boldsymbol{\lambda}^{t}\left(\boldsymbol{x}+\boldsymbol{v}^{t\to \mathbf{0}}\right)\right\|_{l2}^{2} + \beta\varphi\left(\boldsymbol{v}^{t\to \mathbf{0}}\right) \end{aligned} \quad (7)$$

In equation (7), $\boldsymbol{v}^{\mathbf{0}\to t} \circ \boldsymbol{v}^{t\to \mathbf{0}} = 0$, where $\circ$ is a composition operator so that $\boldsymbol{v}^{\mathbf{0}\to t} \circ \boldsymbol{v}^{t\to \mathbf{0}} = \boldsymbol{v}^{\mathbf{0}\to t}(\boldsymbol{x} + \boldsymbol{v}^{\mathbf{0}\to t}) + \boldsymbol{v}^{t\to \mathbf{0}}$. Two cost functions are used to estimate forward and backward deformation under an inverse consistent constraint: $\boldsymbol{v}^{\mathbf{0}\to t} \circ \boldsymbol{v}^{t\to \mathbf{0}} = 0$. In addition, $\boldsymbol{\lambda}^{\mathbf{0}}$ and $\boldsymbol{\lambda}^{t}$ are initially pmc-PET images in phase *0* and *t*, respectively. The first term in the presented cost functions represents data fidelity and calculates the difference between the measured projections and the mathematical projections of the moving images. The second term applies smoothing on the estimated DVF maps:

$$\varphi(v) = \sum_{v \in R^3} \sum_{i=1}^{3} \sum_{j=1}^{3} \left(\frac{\partial v^i}{\partial x^j} \right)^2 \quad (8)$$

The β coefficient controls the amount of smoothness on the estimated motion vectors. Both $\boldsymbol{v}^{\mathbf{0}\rightarrow t}$ and $\boldsymbol{v}^{t\rightarrow \mathbf{0}}$ are calculated by minimizing f_1 and f_2 respectively by an interleaved optimization scheme. In the interleaved optimization scheme, the optimization of f_1 and f_2 was performed alternately at each iteration (Guetter *et al.*, 2011). The solution achieved by this scheme is not necessarily optimal. However, it offers a practical strategy to obtain inverse-consistent DVFs required by the motion-compensated reconstruction step. Cost functions were minimized using the nonlinear conjugate gradient (NLCG) method with a back-tracking line search (Lustig *et al.*, 2007; Wang and Gu, 2013b, a). For the NLCG method, a normal line search method with 10 iterations was used. The initial step size was $\alpha = 1$ and the step reduction coefficient (α_{red}) was 0.2. The stopping criteria, ε, was preset to 10^{-5}. A detailed description of the algorithm was previously demonstrated (Wang and Gu, 2013b). The new DVFs were applied in equations (5) and (6) to reconstruct updated images using an iterative process, with the number of iterations predetermined by the user. The smoothness of the reconstructed image after each sub-iteration was achieved using TV minimization.

2-5. 4D XCAT phantom with respiratory motion

Simulation was performed using a 4D XCAT digital phantom, a realistic whole-body model that represents organ geometry and controls organ motion, based on nonuniform rational B-spline surfaces (NURBS) (Segars *et al.*, 2010). A phantom representing a typical 74 kg male patient with normal FDG levels was generated based on human studies of FDG biodistribution (Zincirkeser *et al.*, 2007; Ramos *et al.*, 2001). Eight 3D activity phantoms were produced during one respiratory cycle. Each phantom corresponded to 0.625 s considering a normal respiratory cycle of 5 s. The first frame represented full exhalation, with the maximum magnitude of respiratory motion (full inhale) occurring between the 4th and 5th frames. The deformation matrices were derived between all individual reconstructed frames (frames 2–8) and the corresponding full exhalation reconstructed frame (i.e. frame 1).

2-6. Tumor Size, Location, and Activity

Lung and liver spherical tumors with diameters ranging from 10 to 40 mm were simulated. For the lung study, tumors were placed near the lung base right above the diaphragm, where motion is higher due to respiration. For every tumor size, lesion to background activity ratios of 2:1, 3:1 and 4:1 were considered, resulting in 21 phantoms with lung lesions. For the liver phantom, tumors were placed in the superior part of the right lobe under the diaphragm, where motion due to respiration is considerably higher. Lesion to background ratios of 2:1 and 3:1 were considered resulting in a total of 14 phantoms with liver tumors. Each phantom was generated in 8 different respiratory phases. A single coronal slice from the XCAT phantom with 15 mm tumors in the liver and lung, and a lesion to background activity ratio of 3 in phase 1 is illustrated in figure 1.

2-7. Physical phantom study

A water filled cylindrical water phantom with two small tubes resembling the tumors was used for 4D-PET imaging. For background activity, 5 mCi FDG were injected into the phantom and diluted with approximately 5000 ml of water. Another 0.5 mCi FDG were injected into two tubes inside the phantom, each of $0.75cm^2 \times 3cm$ in size. This phantom was placed on top of a platform exhibiting sinusoidal motion along the cranial-caudal direction. The amplitude of motion was 1.5 cm with a period of 4.3 s. A total of eight phases was obtained for the 4D-PET study, and the total acquisition time of the 4D-PET was 7 minutes.

2-8. Evaluation parameters

To evaluate the potential of the proposed SMEIR algorithm, tumor volume, tumor to background activity ratio (contrast) and standardized uptake values (SUVs) were compared for the reconstructed images using single frame projections, 3D PET, PRR with Demons-derived DVFs and SMEIR.

The use of standardized uptake values (SUVs) is now common in clinical FDG-PET/CT oncology imaging, and plays a specific role in assessing patient response to cancer therapy. The use of SUVs reduces the variability introduced by differences in patient size and the amount of injected FDG (Kinahan and Fletcher, 2010).

$$SUV = \frac{activity\ concentration\ in\ a\ ROI\ \ (MBq/ml)}{injected\ dose\ \ (MBq)\ /body\ weight\ (g)} \quad (9)$$

SUVs were determined for tumors in all images assuming a 74 kg patient (provided by the phantom developer) and 370MBq of injected FDG, routinely used in clinical practice. SUV values in the XCAT phantom were considered as reference, and the SUV values from the reconstructed images were compared to those from the XCAT phantom. For every image, the mean SUV value (SUV_{mean}) was calculated by considering the mean activity concentration in the delineated tumor volume. For all parameters, the relative error compared to the XCAT values was plotted for different tumor sizes and contrasts.

Tumor delineation was performed based on a background-subtraction method that cancels out the additive effect of background on tumor activity. The equation has been reported as (Hofheinz *et al.*, 2012; Hofheinz *et al.*, 2013):

$$T = k \times (M - Bkg) + Bkg \quad (10)$$

where M is the region of interest (ROI) maximum, Bkg is the mean value in the background ROI, and k represents the required background corrected relative threshold. For homogeneous structures and tumors more than twice as large as the reconstructed image spatial resolution, a fixed value of k = 0.39 (derived from calibration measurements in phantoms) leads to the accurate delineation of the actual boundary; this is independent of the lesion's target to background contrast and shape. A modified voxel based version of the

current algorithm can be used for heterogeneous tumors (Hofheinz *et al.*, 2013). However, since our tumor and background are uniform, we selected the simple method. A 3D cubic ROI covering the entire tumor was considered. Additionally, the same size ROI was considered as background for tumor analysis in lung and liver regions.

3. RESULTS

3-1. High count images

3-1-1. Liver images—A coronal slice of the high-count volumes reconstructed by different methods for three tumor sizes, with a tumor contrast of 2 for input phantoms, is shown in figure 2a. As expected, single phase images (Fig. 2b) were relatively noisy when compared to other images. Since the liver contains a higher amount of activity than the lung, the tumor was relatively hot and less affected by statistical noise. Motion blurring effects were clearly present in 3D-PET images, and were amplified further for smaller tumors (Fig. 2c). As observed in figure 3, 3D-PET images overestimated the tumor volume resulting in a high relative error ranging from +150% for 10 mm diameter tumors to +11% for 40 mm tumors, with a contrast value of 2. The error was even higher for images with higher tumor contrast, ranging from +172% for 10 mm tumors to +21% for 40 mm tumors, with a contrast value of 3. The blurring effect significantly underestimated tumor activity and contrast. The relative error in tumor contrast varied from −38% to −13% depending on tumor size for a contrast of 2, and from −47% to −18% for a contrast of 3 (Fig. 4). The values of SUV_{mean} showed the highest level of deviation from their corresponding reference values in phantoms. The relative error varied with tumor size and ranged from −50% to −30% for a tumor contrast of 2, and from −59% to −35% for a tumor contrast of 3. Both registration methods (Figs. 2d and 2e) dramatically improved the image quality. However, PRR images still suffered from relatively high quantitative errors in determining SUV_{mean}. For example, the PRR relative error was about −10% in contrast recovery and about −30% in the SUV_{mean} calculation (Fig. 4). In contrast, SMEIR using all projection data and motion vectors during reconstruction yielded the best results based on SUV_{mean} and contrast recovery for all tumor sizes and contrasts.

3-1-2. Lung images—Lung image results were more influenced by statistical noise because of the lower activity in the organ and relative tumors compared to high-count liver images. The images reconstructed from the aforementioned methods for three different tumor sizes, with a tumor contrast of 3, are illustrated (Fig. 5). Despite the high count level, single frame images were still noisy, making detection of small and low contrast tumors challenging. A low contrast tumor (contrast value of 2) with a 10 mm diameter was not detectable in 3D, single frame or PRR images is shown in figure 6.

Due to low noise levels, an accurate delineation of tumor volume with single frame images was possible. In contrast, an accurate estimation of the tumor contrast and SUV_{mean} was not feasible with single frame and 3D-PET images. The blurring effect of respiratory motion in 3D-PET images resulted in a 120% overestimation of small tumor volumes. The error was reduced to +20% for larger tumors.

The major challenge in 3D-PET is image quantification. The relative error in contrast estimation was considerably high and ranged from −50% to −18% depending on tumor size (Fig. 7). This error was less sensitive to tumor contrast resulting in similar error curves. A higher relative error was observed in SUV_{mean} values in 3D-PET images, varying from −59% to −30% in tumor size, with lower sensitivity to tumor contrast. SMEIR had the lowest relative error in both contrast and SUV_{mean} estimation among the different motion correction methods. SMEIR resulted in full contrast recovery (less than 5% error) and less than 10% underestimation of SUV_{mean} for tumors with a diameter greater than 20 mm (Fig. 7).

3-2. Low count images

3-2-1. Liver images—A coronal slice of the reconstructed volumes using different methods for three different tumor sizes, with a tumor to background contrast of 2 in input phantoms, is shown (Fig. 8a). As expected, single phase images were noisy as they only contained a portion of the projection data (Fig. 8b). The 3D-PET images were constructed by summing all individual phase images (Fig. 8c). The motion blur can be clearly seen for smaller tumors. In this realistic noise level, the importance of motion correction was observed. While the PRR method considerably improved the image quality (Fig. 8d), tumor contrast could not be recovered. However, the SMEIR method yielded images with a higher tumor contrast while preserving the signal-to-noise-ratio (SNR). Ten millimeter tumors were not detectable in single frame and 3D-PET images for both tumor contrasts (Fig. 9). For lower contrast tumors, even a 15 mm tumor could not be identified in 3D-PET images. Moreover, for detected tumors the relative error in tumor size was considerably high. This was especially true for lower contrast tumor images without motion correction.

Relative errors in tumor contrast and SUV_{mean} values for different reconstruction techniques are presented in figure 10. Tumor quantification and contrast recovery of small tumors were elevated with the SMEIR technique as compared to other methods. Moreover, SMEIR performance was less influenced by tumor size, especially for SUV_{mean} estimation.

3-2-2. Lung images—Lung images were more challenging to obtain since the lower count level in this organ accounts for higher statistical variation. The effects of tumor size and tumor contrast for different reconstructed volumes are shown in figures 11 and 12, respectively. As illustrated in figure 13, for a contrast of 2 tumors smaller than 25 mm were not detectable in single frame and 3D-PET images. However, SMEIR could identify tumors as small as 15 mm with a contrast of 2, and 10 mm for higher contrasts. Moreover, for detected tumors, the relative error in tumor size was considerably high, especially for lower contrast tumor images without motion correction.

Based on contrast recovery and SUV_{mean}, the PRR method performance was comparable with single frame images (Fig. 14). However, the SMEIR method yielded improved tumor quantification when compared to other systems. For example, for 20 mm tumor with a contrast of 3, the contrast relative error was reduced to −4% when using SMEIR from −42% with the other three methods (3D-PET, single frame and PRR). For the same set of images,

the SUV_{mean} value relative error was reduced from −51% in other methods (3D-PET, single frame and PRR) to −12% in our proposed SMEIR method.

3-3. Physical phantom images

The reconstructed images of the two different individual phases are illustrated in figure 15. The effect of motion can be seen in both sagittal and coronal planes. Moreover, tumors are less visible in the transverse plane of phase 0 because they shifted out of view in this slice. The 4D-PET reconstructed images using the PRR and SMEIR methods and the 3D-PET in transverse, coronal, and sagittal views are indicated in figure 16.

Pixel values across the horizontal line passing from the center of the hot tube in different images are displayed in figure 17. Axial motion resulted in the broadening of the tumor in 3D-PET images, increasing the volume and decreasing the activity concentration (Figure 17). Both PRR and SMEIR methods recovered the shape of the tumor; however, line profiles show that SMEIR outperforms PRR.

4. DISCUSSION AND CONCLUSION

In this study, we investigated an iterative algorithm for simultaneous motion estimation and image reconstruction in 4D-PET. The proposed algorithm only used 4D-PET projection data as compared to previous methods based on external markers or complementary dynamic CT/MR images for motion estimation. The proposed SMEIR algorithm estimates motion vectors by matching the projections of the deformed reconstructed image to projections from other phases. Moreover, SMEIR uses all projection data to reconstruct a particular phase image by explicitly considering the motion model between different phases. Therefore, SMEIR can effectively suppress noise and increase image reconstruction accuracy. In our implementation, the motion-compensated image reconstruction step was performed by applying motion vectors in a hybrid, intuitive reconstruction algorithm that replaced the OSEM algorithm. Our results showed that approximating deformation matrix and its transpose in equation 6 by forward and backward warping functions is capable to reconstruct motion-freeze 4D-PET images. This approximation is absolutely correct for rigid transformation where the deformation matrix is orthogonal and there is a one-to-one correspondence between the reference and the deformed images. Using inverse operator instead of transpose matrix for non-rigid transformation has been shown to be still an acceptable approximation. Li et al. also used the same approximation for 4D-PET image reconstruction in which forward and backward warping operators replaced the deformation matrix and its transpose. They also illustrated the convergence of the algorithm by plotting tumor uptake value as a function of iteration number (Li *et al.*, 2006). To obtain inverse consistent forward and backward DVFs in the motion estimation step, we alternatingly minimized two objective functions to calculate the difference between the measured projections and the mathematical projections of the moving images. Thus, the presented SMEIR method is an ad hoc but practical algorithm. Alternatively, the DVFs and the PET image can be estimated by maximizing a single objective function in an alternating way (Wang and Qi, 2015; Blume *et al.*, 2010).

The accuracy of the final reconstructed images is highly affected by motion estimation accuracy. Assuming object diffeomorphic motion during the scan, we estimated the initial DVF by reconstructing an individual 4D-PET phase using OSEM+TV, and performing the inverse consistent Demons deformable image registration between different phases of 4D-PET. The initial DVF was then refined by minimizing equation (7) to obtain the updated motion model. Since a large number of DVF unknowns are required to be solved from a limited number of projections, equation (7) defines an ill-posed problem and is very sensitive to the initialization of DVFs. To avoid convergence to local minima minimum instead of the desired global minimum, we used Demons-derived DVFs as an initial acceptable estimate of the actual DVFs. When compared to single frame image and 3D-PET, the PRR method using Demons DVFs showed significant improvements in image quality and quantification. An additional improvement was achieved by refining DVFs in equation (10) for the SMEIR algorithm. Results obtained with SMEIR were more encouraging than those observed with PRR for two reasons: 1) SMEIR uses DVFs during image reconstruction along with all projection data for each iteration; 2) SMEIR tunes Demons-derived DVFs by matching projections, resulting in higher accuracy.

In our ill-posed inverse problem, regularization is needed for all parameters subjected to estimation (i.e. image and motion). Many image regularization techniques have been proposed in the literature. Examples include the use of a 3D isotropic Gaussian smoothing after each image update (Blume *et al.*, 2012) and a roughness penalty in the reconstruction algorithm (Jacobson and Fessler, 2003). However, when the roughness penalty is included in the reconstruction algorithm, the tumor and nearby regions should be excluded from it for better tumor quantification (Jacobson and Fessler, 2006). Jacobson and Fessler employed a scheme based on CT side-information to identify the location of the tumor, and used an ROI covering the tumor and nearby regions to exclude them from the roughness penalty. They showed that when a roughness penalty is uniformly applied to the image, the efficiency of the tumor activity recovery is reduced as compared with the simple PRR method (Jacobson and Fessler, 2006). However, the use of CT side information and the exclusion of the tumor region from the penalty improved theactivity recovery (Jacobson and Fessler, 2006). We used TV minimization after each sub-iteration as a surrogate for Gaussian filtering to suppress noise, preserve tumor shape and edges, and prevent the blur of tumors to be quantified (Panin *et al.*, 1999; Setzer *et al.*, 2010; Brune *et al.*, 2009; Persson *et al.*, 2001). Our results are comparable with the Jacobson and Fessler method in terms of CT side information. However our SMEIR method outperforms their joint estimation algorithm without CT side data based on lesion recovery values. They reported a 17% improvement in lesion recovery using their joint estimation algorithm as compared to the PRR method, where CT side data is available. We also showed that for small tumors (10 mm and 15 mm), the SMEIR method dramatically improved lesion recovery (SUV_{mean}) as compared to PRR (Figs.10 and 14) without using any side data. For 10 mm tumors with a contrast of 3, the relative errors in (SUV_{mean}) were reduced by 38% and 18% in low-count liver and lung images, respectively.

Liver image results showed that while both registration methods yielded a similar tumor size, especially for a tumor contrast of 3 (Figs. 2 and 8), considerable differences can be detected in terms of quantitative values (i.e. contrast and SUV_{mean}) (Figs. 4 and 10). While

all reconstruction methods underestimated SUV_{mean} compared to phantom data, this difference was considerably lower in the SMEIR method (<10%) for all tumor sizes and contrasts (Figure 10). Moreover, the SMEIR-derived SUV_{mean} values were less sensitive to tumor size and noise levels. As observed in figures 4 and 10, SMEIR plots were less sensitive to tumor size for both noise levels. This can be very important because SUV_{mean} is being widely used as a semi quantitative parameter to differentiate between malignant and benign lesions, determine disease stage, and monitor response to treatment. SUV_{mean} should be independent of tumor size and measure tumor uptake; these characteristics are improved with the SMEIR method as compared to other reconstruction methods. Our lung image results suggest that the minimum detectable combination of tumor size and contrast depends on the reconstruction algorithm. Only SMEIR was able to accurately detect 10 mm tumors with a contrast of 2 in high count images (Fig. 6). For low count images (Fig. 13), the 3D-PET and single frame methods were unable to accurately detect low contrast tumors smaller than 25 mm. However, PRR could identify 20 mm tumors, while SMEIR detected tumors as small as 15 mm at a contrast of 2. Both registration methods could accurately detect the tumor size, however, based on the quantitative analysis of contrast and SUV_{mean}, the smallest number of errors was determined from images reconstructed by the SMEIR algorithm (Figs. 7 and 14). Our studies indicate that the SMEIR method significantly improves tumor detection and quantification while reducing motion related artifacts and errors. Additionally, we showed that the PRR method based on Demons-derived DVFs was unable to fully recover contrast and SUV_{mean} even with high count projections.

In a recent study, investigators used an integrated PET/MRI system in which the motion model was derived from gated high resolution MR images and applied to 4D-PET images for motion correction using the PRR method. This study was conducted on 39 lung cancer patients. The Gated reconstruction using 40% of the data with the smallest amount of variation was considered as the reference image. They reported an average of 5% reduction in the SUV_{mean} error using their approach compared with 3D-PET images (Grimm *et al.*, 2015). We showed that PRR performed slightly better than 3D-PET, although the SMEIR method significantly outperformed PRR for different tumor sizes and contrasts (Figs. 7 and 14). Assuming that MRI provides high accuracy motion models, model-based reconstruction methods, where the motion field is incorporated directly into the PET reconstruction, may show higher quantitative accuracy compared with PRR methods. In another simulation study, Guérin et al. reported that incorporating an MRI-derived motion field in EM reconstruction improves the contrast recovery from about 45% to 70% for small liver tumors with a 25% error reduction (Guerin *et al.*, 2011). We showed a 25% error reduction in contrast recovery using SMEIR for 10 mm tumors with a contrast of 2, as indicated in figure 10.

In this study, we evaluated the SMEIR algorithm on a digital 4D XCAT phantom with uniform activity in each organ during a regular respiratory cycle. While promising results were obtained in the phantom simulation study, additional studies are needed to confirm the effectiveness of the method for clinical use. Additionally, several parameters in the SMEIR algorithm including the β value and TV smoothing parameters were selected empirically. Future studies are required to optimize these parameters and improve the performance of the SMEIR algorithm in real 4D-PET images.

ACKNOWLEDGMENTS

We acknowledge funding support from the American Cancer Society (RSG-13-326-01-CCE), the US National Institutes of Health (R01 EB020366) and the Cancer Prevention and Research Institute of Texas (RP130109). We would like to thank Dr. Damiana Chiavolini for editing the paper.

REFERENCES

Blume M, Martinez-Moller A, Keil A, Navab N, Rafecas M. Joint reconstruction of image and motion in gated positron emission tomography. IEEE transactions on medical imaging. 2010; 29:1892–906. [PubMed: 20562034]

Blume M, Navab N, Rafecas M. Joint image and motion reconstruction for PET using a B-spline motion model. Physics in medicine and biology. 2012; 57:8249–70. [PubMed: 23190499]

Brune C, Sawatzky A, Burger M. Bregman-EM-TV Methods with Application to Optical Nanoscopy. Lect Notes Comput Sc. 2009; 5567:235–46.

Bruyant PP. Analytic and iterative reconstruction algorithms in SPECT. Journal of nuclear medicine : official publication, Society of Nuclear Medicine. 2002; 43:1343–58.

Cai J, Chang Z, Wang Z, Paul Segars W, Yin FF. Four-dimensional magnetic resonance imaging (4D-MRI) using image-based respiratory surrogate: a feasibility study. Medical physics. 2011; 38:6384–94. [PubMed: 22149822]

Callahan J, Kron T, Siva S, Simoens N, Edgar A, Everitt S, Schneider ME, Hicks RJ. Geographic miss of lung tumours due to respiratory motion: a comparison of 3D vs 4D PET/CT defined target volumes. Radiation oncology. 2014; 9:291. [PubMed: 25511904]

Chua SC, Groves AM, Kayani I, Menezes L, Gacinovic S, Du Y, Bomanji JB, Ell PJ. The impact of 18F-FDG PET/CT in patients with liver metastases. European journal of nuclear medicine and molecular imaging. 2007; 34:1906–14. [PubMed: 17713766]

Chun SY, Reese TG, Ouyang J, Guerin B, Catana C, Zhu X, Alpert NM, El Fakhri G. MRI-based nonrigid motion correction in simultaneous PET/MRI. Journal of nuclear medicine : official publication, Society of Nuclear Medicine. 2012; 53:1284–91.

Cohade C, Osman M, Marshall LN, Wahl RN. PET-CT: accuracy of PET and CT spatial registration of lung lesions. European journal of nuclear medicine and molecular imaging. 2003; 30:721–6. [PubMed: 12612809]

Dang J, Gu X, Pan T, Wang J. A pilot evaluation of a 4-dimensional cone-beam computed tomographic scheme based on simultaneous motion estimation and image reconstruction. International journal of radiation oncology, biology, physics. 2015; 91:410–8.

Dawood M, Buther F, Jiang X, Schafers KP. Respiratory motion correction in 3-D PET data with advanced optical flow algorithms. IEEE transactions on medical imaging. 2008; 27:1164–75. [PubMed: 18672433]

Dawood M, Lang N, Jiang X, Schafers KP. Lung motion correction on respiratory gated 3-D PET/CT images. IEEE transactions on medical imaging. 2006; 25:476–85. [PubMed: 16608062]

Erdi YE, Nehmeh SA, Pan T, Pevsner A, Rosenzweig KE, Mageras G, Yorke ED, Schoder H, Hsiao W, Squire OD, Vernon P, Ashman JB, Mostafavi H, Larson SM, Humm JL. The CT motion quantitation of lung lesions and its impact on PET-measured SUVs. Journal of nuclear medicine : official publication, Society of Nuclear Medicine. 2004; 45:1287–92.

Erdi YE, Rosenzweig K, Erdi AK, Macapinlac HA, Hu YC, Braban LE, Humm JL, Squire OD, Chui CS, Larson SM, Yorke ED. Radiotherapy treatment planning for patients with non-small cell lung cancer using positron emission tomography (PET). Radiotherapy and oncology : journal of the European Society for Therapeutic Radiology and Oncology. 2002; 62:51–60. [PubMed: 11830312]

Fayad H, Schmidt H, Wurslin C, Visvikis D. Reconstruction incorporated respiratory motion correction in clinical simultaneous PET/MR imaging for oncology applications. Journal of nuclear medicine : official publication, Society of Nuclear Medicine. 2015

Gambhir SS, Czernin J, Schwimmer J, Silverman DH, Coleman RE, Phelps ME. A tabulated summary of the FDG PET literature. Journal of nuclear medicine : official publication, Society of Nuclear Medicine. 2001; 42:1S–93S.

Geramifar P, Zafarghandi MS, Ghafarian P, Rahmim A, Ay MR. Respiratory-induced errors in tumor quantification and delineation in CT attenuation-corrected PET images: effects of tumor size, tumor location, and respiratory trace: a simulation study using the 4D XCAT phantom. Molecular imaging and biology : MIB : the official publication of the Academy of Molecular Imaging. 2013; 15:655–65. [PubMed: 23780352]

Goerres GW, Burger C, Schwitter MR, Heidelberg TN, Seifert B, von Schulthess GK. PET/CT of the abdomen: optimizing the patient breathing pattern. European radiology. 2003; 13:734–9. [PubMed: 12664111]

Grimm R, Furst S, Souvatzoglou M, Forman C, Hutter J, Dregely I, Ziegler SI, Kiefer B, Hornegger J, Block KT, Nekolla SG. Self-gated MRI motion modeling for respiratory motion compensation in integrated PET/MRI. Medical image analysis. 2015; 19:110–20. [PubMed: 25461331]

Gu X, Pan H, Liang Y, Castillo R, Yang D, Choi D, Castillo E, Majumdar A, Guerrero T, Jiang SB. Implementation and evaluation of various demons deformable image registration algorithms on a GPU. Physics in medicine and biology. 2010; 55:207–19. [PubMed: 20009197]

Guerin B, Cho S, Chun SY, Zhu X, Alpert NM, El Fakhri G, Reese T, Catana C. Nonrigid PET motion compensation in the lower abdomen using simultaneous tagged-MRI and PET imaging. Medical physics. 2011; 38:3025–38. [PubMed: 21815376]

Guetter, C.; Xue, H. Chefd'hotel C and Guehring J. IEEE International Symposium on Biomedical Imaging; 2011. p. 590-3.vol. Series)

Han, GP.; Liang, ZR.; You, JS. A fast ray-tracing technique for TCT and ECT studies. Ieee Nucl Sci Conf R; 1999. p. 1515-8.

Hofheinz F, Langner J, Petr J, Beuthien-Baumann B, Steinbach J, Kotzerke J, van den Hoff J. An automatic method for accurate volume delineation of heterogeneous tumors in PET. Medical physics. 2013; 40:082503. [PubMed: 23927348]

Hofheinz F, Potzsch C, Oehme L, Beuthien-Baumann B, Steinbach J, Kotzerke J, van den Hoff J. Automatic volume delineation in oncological PET. Evaluation of a dedicated software tool and comparison with manual delineation in clinical data sets *Nuklearmedizin*. Nuclear medicine. 2012; 51:9–16. [PubMed: 22027997]

Hudson HM, Larkin RS. Accelerated image reconstruction using ordered subsets of projection data. IEEE transactions on medical imaging. 1994; 13:601–9. [PubMed: 18218538]

Jacobson, MW.; Fessler, JA. Joint estimation of image and deformation parameters in motion-corrected PET. PET IEEE Nuclear Science Symp; 2003. p. 3290-4.

Jacobson, MW.; Fessler, JA. Joint estimation of respiratory motion and activity in 4D PET using CT side information. I S Biomed Imaging; 2006. p. 275-8.

Kinahan PE, Fletcher JW. Positron emission tomography-computed tomography standardized uptake values in clinical practice and assessing response to therapy. Seminars in ultrasound, CT, and MR. 2010; 31:496–505.

Kroon, D-J. multimodality non-rigid demon algorithm image registration. 2008.

Lamare F, Cresson T, Savean J, Le Rest CC, Reader AJ, Visvikis D. Respiratory motion correction for PET oncology applications using affine transformation of list mode data. Physics in medicine and biology. 2007a; 52:121–40. [PubMed: 17183132]

Lamare F, Ledesma Carbayo MJ, Cresson T, Kontaxakis G, Santos A, Le Rest CC, Reader AJ, Visvikis D. List-mode-based reconstruction for respiratory motion correction in PET using non-rigid body transformations. Physics in medicine and biology. 2007b; 52:5187–204. [PubMed: 17762080]

Lange K, Carson R. EM reconstruction algorithms for emission and transmission tomography. Journal of computer assisted tomography. 1984; 8:306–16. [PubMed: 6608535]

Li T, Thorndyke B, Schreibmann E, Yang Y, Xing L. Model-based image reconstruction for four-dimensional PET. Medical physics. 2006; 33:1288–98. [PubMed: 16752564]

Lustig M, Donoho D, Pauly JM. Sparse MRI: The application of compressed sensing for rapid MR imaging. Magnetic resonance in medicine. 2007; 58:1182–95. [PubMed: 17969013]

Mah K, Caldwell CB, Ung YC, Danjoux CE, Balogh JM, Ganguli SN, Ehrlich LE, Tirona R. The impact of (18)FDG-PET on target and critical organs in CT-based treatment planning of patients with poorly defined non-small-cell lung carcinoma: a prospective study. International journal of radiation oncology, biology, physics. 2002; 52:339–50.

Manber R, Thielemans K, Hutton B, Barnes A, Ourselin S, Arridge S, O'Meara C, Wan S, Atkinson D. Practical PET Respiratory Motion Correction in Clinical PET/MR. Journal of nuclear medicine : official publication, Society of Nuclear Medicine. 2015

Matsuzaki Y, Fujii K, Kumagai M, Tsuruoka I, Mori S. Effective and organ doses using helical 4DCT for thoracic and abdominal therapies. J Radiat Res. 2013; 54:962–70. [PubMed: 23603303]

Nehmeh SA, Erdi YE, Ling CC, Rosenzweig KE, Schoder H, Larson SM, Macapinlac HA, Squire OD, Humm JL. Effect of respiratory gating on quantifying PET images of lung cancer. Journal of nuclear medicine : official publication, Society of Nuclear Medicine. 2002; 43:876–81.

Nehmeh SA, Erdi YE, Rosenzweig KE, Schoder H, Larson SM, Squire OD, Humm JL. Reduction of respiratory motion artifacts in PET imaging of lung cancer by respiratory correlated dynamic PET: methodology and comparison with respiratory gated PET. Journal of nuclear medicine : official publication, Society of Nuclear Medicine. 2003; 44:1644–8.

Osman MM, Cohade C, Nakamoto Y, Wahl RL. Respiratory motion artifacts on PET emission images obtained using CT attenuation correction on PET-CT. European journal of nuclear medicine and molecular imaging. 2003; 30:603–6. [PubMed: 12536242]

Panin VY, Zeng GL, Gullberg GT. Total variation regulated EM algorithm. Ieee T Nucl Sci. 1999; 46:2202–10.

Park SJ, Ionascu D, Killoran J, Mamede M, Gerbaudo VH, Chin L, Berbeco R. Evaluation of the combined effects of target size, respiratory motion and background activity on 3D and 4D PET/CT images. Physics in medicine and biology. 2008; 53:3661–79. [PubMed: 18562782]

Persson M, Bone D, Elmqvist H. Total variation norm for three-dimensional iterative reconstruction in limited view angle tomography. Physics in medicine and biology. 2001; 46:853–66. [PubMed: 11277230]

Polycarpou I, Tsoumpas C, King AP, Marsden PK. Impact of respiratory motion correction and spatial resolution on lesion detection in PET: a simulation study based on real MR dynamic data. Physics in medicine and biology. 2014; 59:697–713. [PubMed: 24442386]

Qiao F, Pan T, Clark JW Jr. Mawlawi OR. A motion-incorporated reconstruction method for gated PET studies. Physics in medicine and biology. 2006; 51:3769–83. [PubMed: 16861780]

Rahmim, A.; Tang, J.; Ay, MR.; Bengel, FM. 4D Respiratory Motion-Corrected Rb-82 Myocardial Perfusion PET Image Reconstruction. 2010 Ieee Nuclear Science Symposium Conference Record (Nss/Mic); 2010. p. 3312-6.

Rahmim A, Tang J, Zaidi H. Four-Dimensional Image Reconstruction Strategies in Cardiac-Gated and Respiratory-Gated PET Imaging. PET Clinics. 2013; 8:51–67. [PubMed: 27157815]

Ramos CD, Erdi YE, Gonen M, Riedel E, Yeung HW, Macapinlac HA, Chisin R, Larson SM. FDG-PET standardized uptake values in normal anatomical structures using iterative reconstruction segmented attenuation correction and filtered back-projection. European journal of nuclear medicine. 2001; 28:155–64. [PubMed: 11303885]

Schwarz AJ, Leach MO. Implications of respiratory motion for the quantification of 2D MR spectroscopic imaging data in the abdomen. Physics in medicine and biology. 2000; 45:2105–16. [PubMed: 10958183]

Segars WP, Sturgeon G, Mendonca S, Grimes J, Tsui BM. 4D XCAT phantom for multimodality imaging research. Medical physics. 2010; 37:4902–15. [PubMed: 20964209]

Seppenwoolde Y, Shirato H, Kitamura K, Shimizu S, van Herk M, Lebesque JV, Miyasaka K. Precise and real-time measurement of 3D tumor motion in lung due to breathing and heartbeat, measured during radiotherapy. International journal of radiation oncology, biology, physics. 2002; 53:822–34.

Setzer S, Steidl G, Teuber T. Deblurring Poissonian images by split Bregman techniques. J Vis Commun Image R. 2010; 21:193–9.

Shepp LA, Vardi Y. Maximum likelihood reconstruction for emission tomography. IEEE transactions on medical imaging. 1982; 1:113–22. [PubMed: 18238264]

Siddon RL. Fast Calculation of the Exact Radiological Path for a 3-Dimensional Ct Array. Medical physics. 1985; 12:252–5. [PubMed: 4000088]

Thirion JP. Image matching as a diffusion process: an analogy with Maxwell's demons. Medical image analysis. 1998; 2:243–60. [PubMed: 9873902]

Toloza EM, Harpole L, McCrory DC. Noninvasive staging of non-small cell lung cancer: a review of the current evidence. Chest. 2003; 123:137S–46S. [PubMed: 12527573]

Wang, G.; Qi, J. A Monotonic Image-Space Algorithm for Joint PET Image Reconstruction and Motion Estimation. IEEE NSS-MIC; San Diego, CA. 2015.

Wang J, Gu X. High-quality four-dimensional cone-beam CT by deforming prior images. Physics in medicine and biology. 2013a; 58:231–46. [PubMed: 23257113]

Wang J, Gu X. Simultaneous motion estimation and image reconstruction (SMEIR) for 4D cone-beam CT. Medical physics. 2013b; 40:101912. [PubMed: 24089914]

Zincirkeser S, Sahin E, Halac M, Sager S. Standardized uptake values of normal organs on 18F-fluorodeoxyglucose positron emission tomography and computed tomography imaging. The Journal of international medical research. 2007; 35:231–6. [PubMed: 17542410]

Figure 1.
A coronal slice of the XCAT phantom with 15 mm tumor in the liver (left) and lung (right), and lesion to background activity ratio of 3 in phase 1 (full exhale).

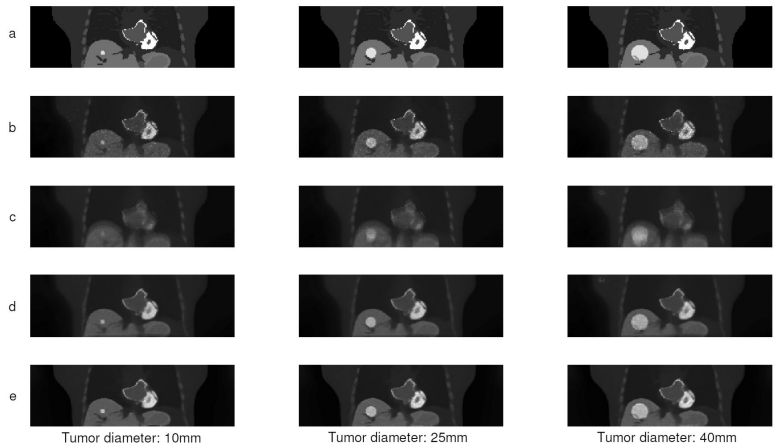

Figure 2.

Effect of tumor size on different reconstructed high count images: a) XCAT Phantom as reference, b) a single frame, c) 3D PET, d) PRR, e) SMEIR. The tumor to background activity ratio was calculated as 2 for all images. The tumor diameter was 10, 25 and 40 mm from left to right, respectively.

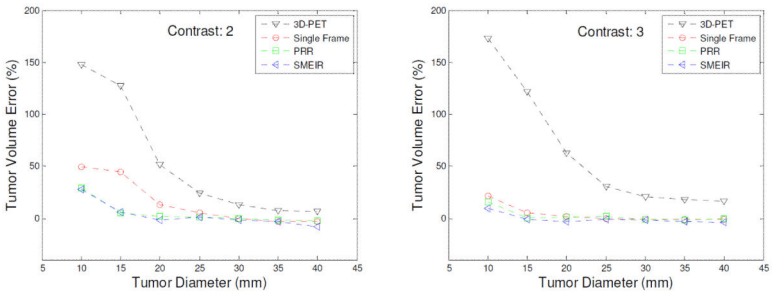

Figure 3.

Tumor volume relative error for different reconstruction methods in high count liver images, with two different tumor to background contrast ratios of 2 (left) and 3 (right).

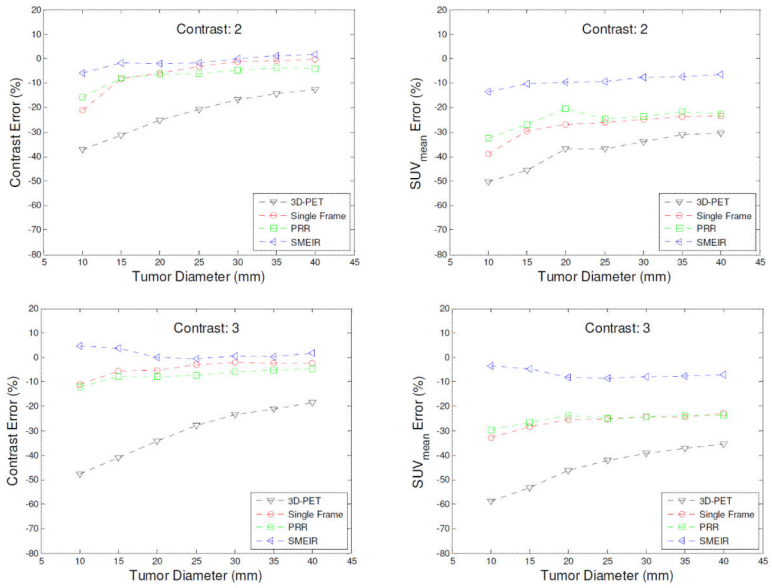

Figure 4.

Relative errors on tumor to background contrast (left column) and mean SUV values (right column) for different reconstruction methods in high count liver images of phantom, with two different tumor to background contrast ratios of 2 (top) and 3 (bottom)

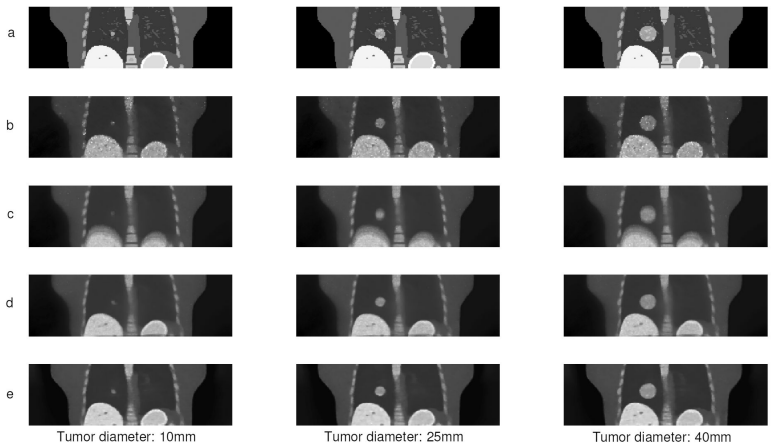

Figure 5.

Effect of tumor size on different reconstructed high count lung images: a) XCAT Phantom, b) a single frame, c) 3D-PET, d) PRR using Demons DVFs, e) SMEIR. The tumor to background contrast was 3 for all images.

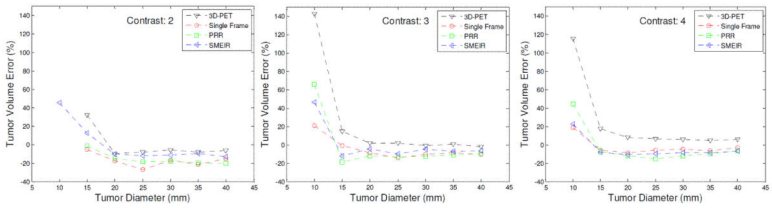

Figure 6.

Tumor volume relative errors for different reconstruction methods in lung images with tumor contrast values of 2 (left), 3 (middle) and 4 (right).

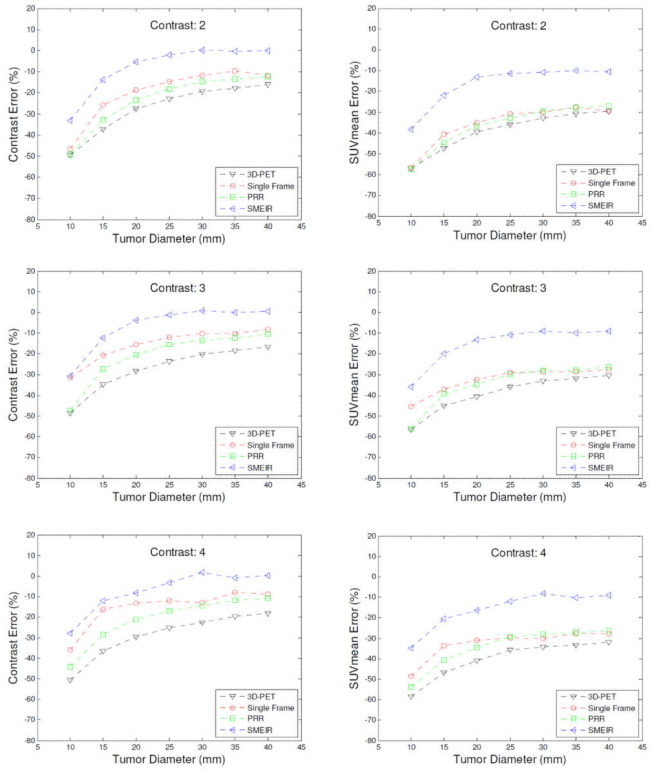

Figure 7.

Relative errors in measured tumor contrast (left column) and SUV_{mean} (right column) in lung images reconstructed by different methods. The tumor contrasts in phantoms were 2 (top), 3 (middle) and 4 (bottom).

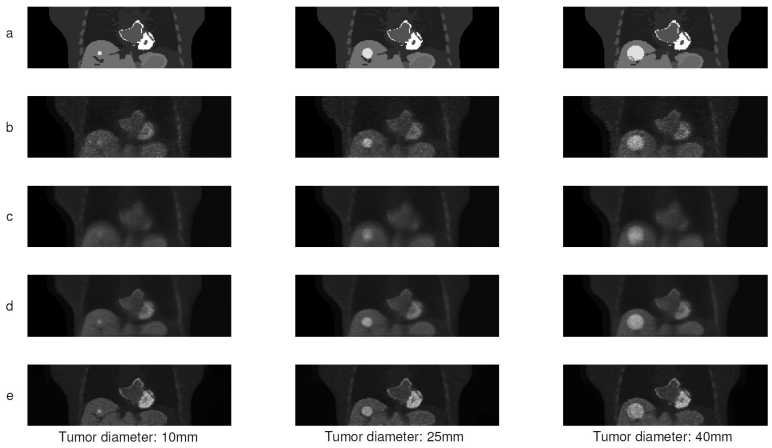

Figure 8.

Effect of tumor size on different reconstructed low count liver images: a) XCAT Phantom, b) a single frame, c) 3D-PET, d) PRR using Demons DVFs, e) SMEIR. The tumor to background contrast was 2 for all images.

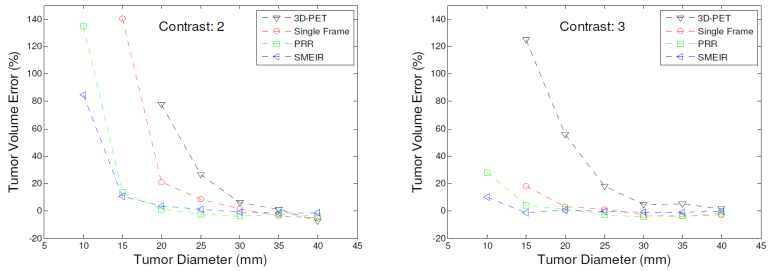

Figure 9.

Tumor volume relative error for different reconstruction methods in low count liver images with two different tumor to background contrast ratios of 2 (left) and 3 (right).

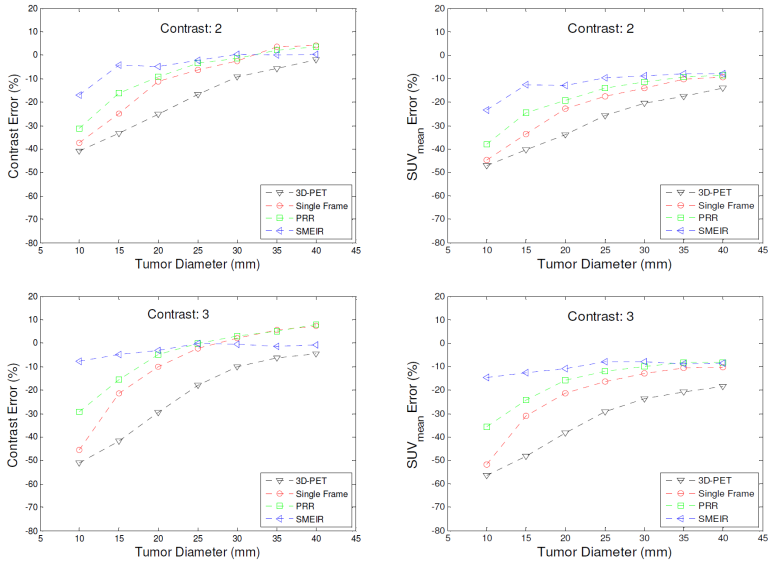

Figure 10.

Relative error on tumor to background contrast (left column) and SUV_{mean} values (right column) for different reconstruction methods in low count liver images of phantom, with two different tumor to background contrasts of 2 (top) and 3 (bottom)

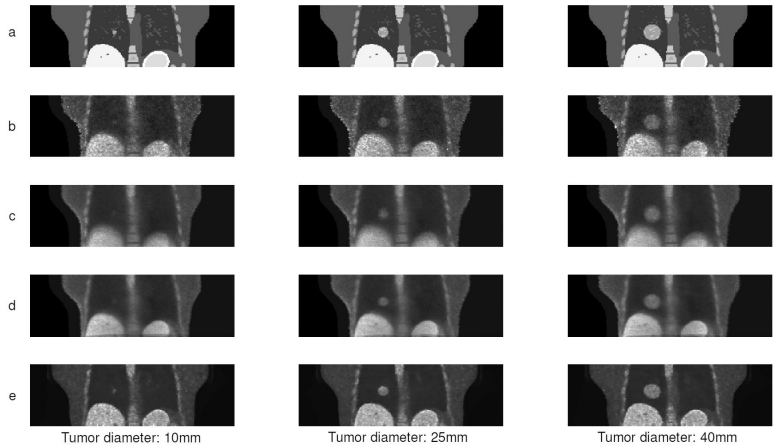

Figure 11.

Effect of tumor size on different reconstructed low count lung images: a) XCAT Phantom, b) a single frame, c) 3D-PET, d) PRR using Demons DVFs, e) SMEIR. The tumor to background contrast was 3 for all images.

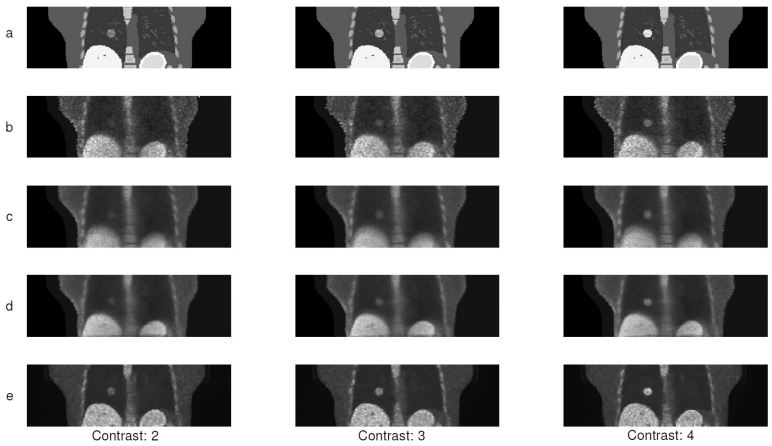

Figure 12.

Effect of tumor to background contrast on different reconstructed low count images with a 20mm tumor in lung: a) XCAT Phantom as reference, b) a single frame, c) 3D-PET, d) PRR, and e) SMEIR.

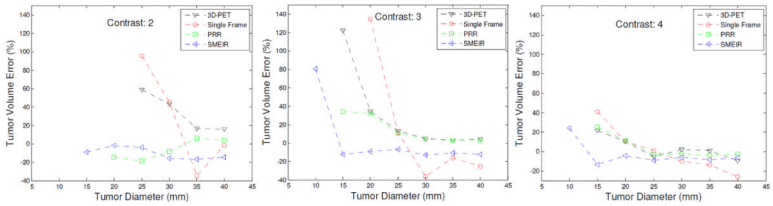

Figure 13.

Tumor volume relative error for different reconstruction methods in noisy lung images with three different tumor contrast of 2 (left), 3 (middle) and 4 (right).

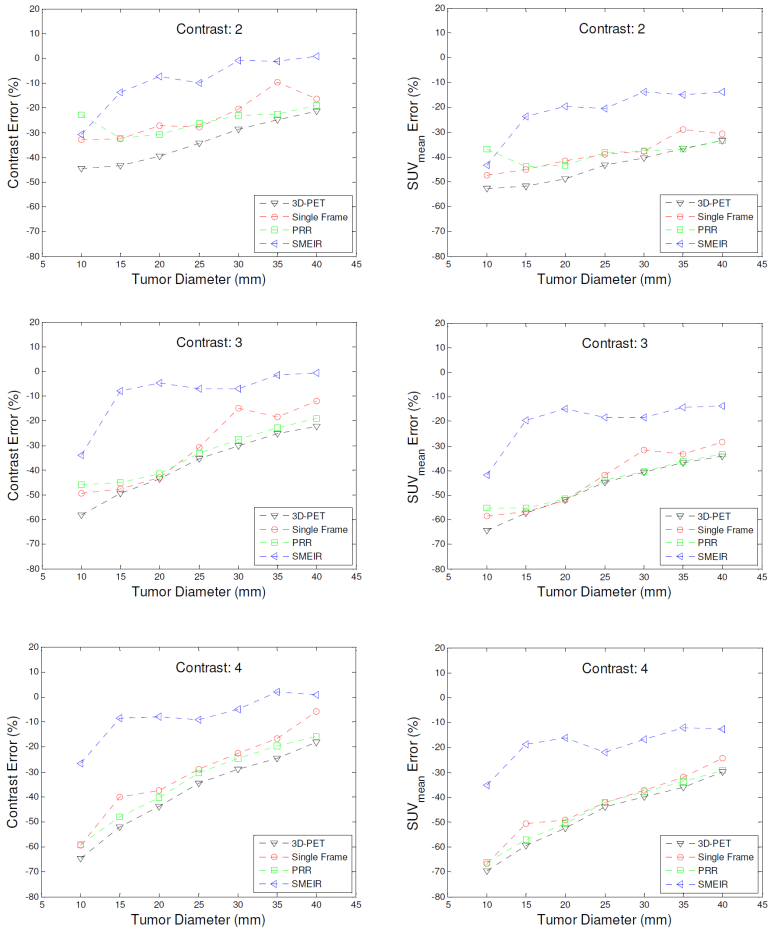

Figure 14.

Relative error on tumor to background contrast (left column) and SUV_{mean} values (right column) for different reconstruction methods in low count lung phantom images, with two different tumor to background contrasts of 2 (top) and 3 (bottom)

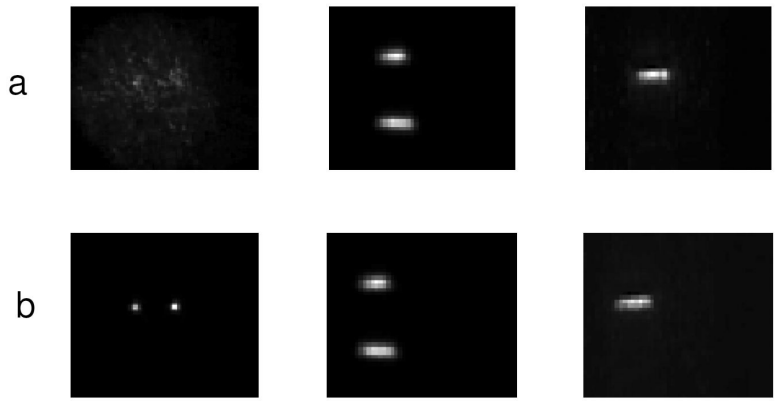

Figure 15.

Reconstructed images of two different individual phases. a) phase 0 image and b) phase 3 image. Tumors are less visible in the transverse view of phase 0 because they had shifted out of view in this slice.

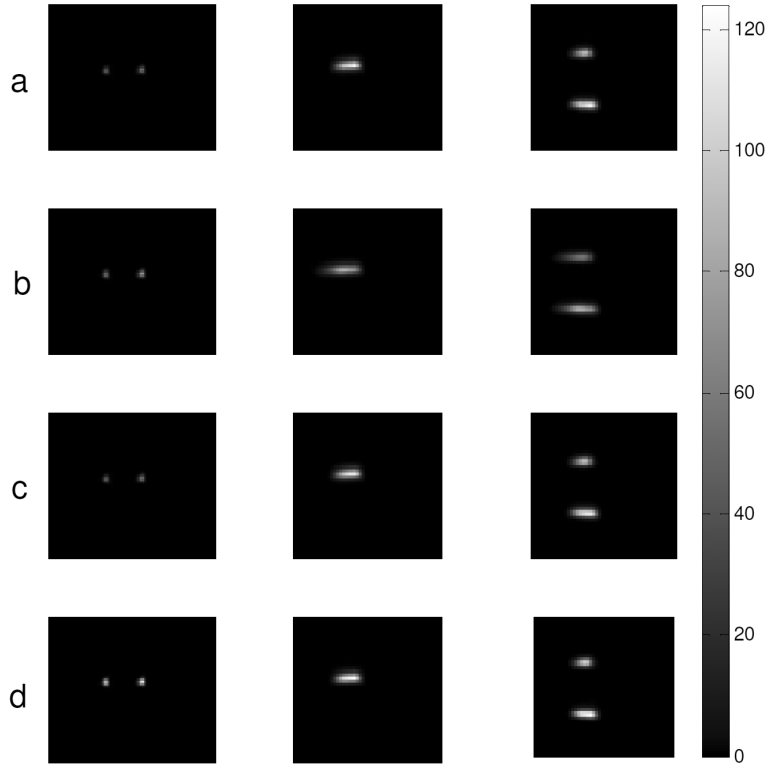

Figure 16.
Reconstructed images of the physical phantom using different methods: a) a single frame, b) 3D-PET, c) PRR using Demons DVFs, d) SMEIR

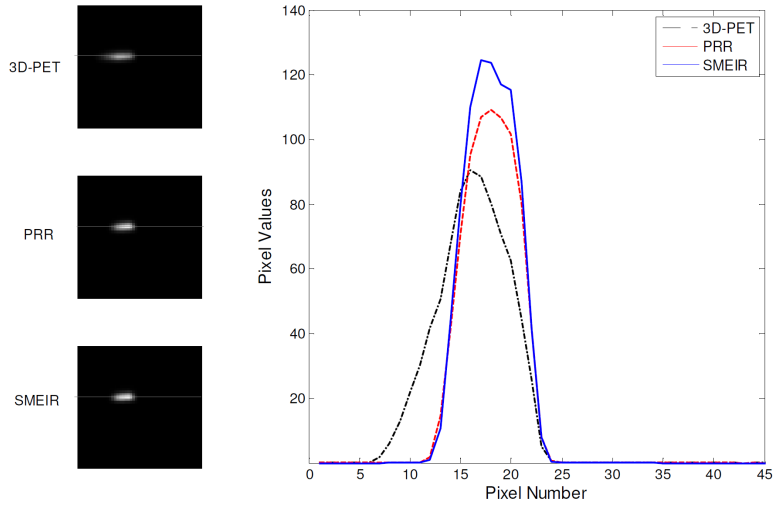

Figure 17.

Horizontal line profiles across the hot tube indicated by the lines in the left for 3D PET, PRR and SMEIR